

On-axis spatially resolved spectroscopy of low redshift quasar host galaxies: HE 1503+0228, at $z = 0.135$ *

F. Courbin^{1,2}, G. Letawe¹, P. Magain¹, L. Wisotzki³, P. Jablonka⁴, K. Jahnke⁵, B. Kuhlbrodt⁵, D. Alloin⁶, G. Meylan⁷, D. Minniti², and I. Burud⁷

¹ Institut d'Astrophysique et de Géophysique, Université de Liège, Allée du 6 Août, 17, Sart Tilman (Bat. B5C), Liège 1, Belgium

² Universidad Católica de Chile, Departamento de Astronomía y Astrofísica, Casilla 306, Santiago 22, Chile

³ Institut für Physik, Universität Potsdam, Am Neuen Palais 10, 14469 Potsdam, Germany

⁴ GEPI, Observatoire de Paris, Place Jules Janssen, F-92915 Meudon Cedex, France

⁵ Hamburger Sternwarte, Universitaet Hamburg, Gojenbergsweg 112, D-21029 Hamburg, Germany

⁶ European Southern Observatory, Casilla 19, Santiago, Chile

⁷ Space Telescope Science institute, 3700 San Martin Drive, Baltimore, MD 21218 USA

Abstract. We present the first result of a comprehensive spectroscopic study of quasar host galaxies. On-axis, spatially resolved spectra of low redshift quasars have been obtained with FORS1, mounted on the 8.2m ESO Very Large Telescope, Antu. The spectra are *spatially deconvolved* using a spectroscopic version of the “MCS deconvolution algorithm”. The algorithm decomposes two dimensional spectra into the individual spectra of the central point-like nucleus and of its host galaxy. Applied to HE 1503+0228 at $z = 0.135$ ($M_B = -23.0$), it provides us with the spectrum of the host galaxy between 3600Å and 8500Å (rest-frame), at a mean resolving power of 700. The data allow us to measure several of the important Lick indices. The stellar populations and gas ionization state of the host galaxy of HE 1503+0228 are very similar to the ones measured for normal non-AGN galaxies. Dynamical information is also available for the gas and stellar components of the galaxy. Using deconvolution and a deprojection algorithm, velocity curves are derived for emission lines, from the center up to 4'' away from the nucleus of the galaxy. Fitting a simple three-components mass model (point mass, spherical halo of dark matter, disk) to the position-velocity diagram, we infer a mass of $M(r < 1\text{kpc}) = (2.0 \pm 0.3)10^{10} M_\odot$ within the central kiloparsec of the galaxy, and a mass integrated over 10 kpc of $M(r < 10\text{kpc}) = (1.9 \pm 0.3)10^{11} M_\odot$, with an additional 10% error due to the uncertainty on the inclination of the galaxy. This, in combination with the analysis of the stellar populations indicates that the host galaxy of HE 1503+0228 is a normal spiral galaxy.

Key words. Galaxies: dynamics, stellar populations – quasars: individual: HE 1503+0228 – techniques: deconvolution

1. Introduction

Luminous quasars are now known to be generally located at the cores of large galaxies. With the recent discovery that supermassive black holes appear to reside in most if not all galaxies with substantial bulges (e.g., Magorrian et al. 1998), it is now quite likely that quasar-like activity is an extremely common but transient phenomenon, linking the growth of now extinct black holes to the violent processes during phases of active accretion (cf. McLeod et al. 1999). However, very little of the physical processes oper-

ating during such episodes of nuclear activity is actually understood: neither do we know the actual conditions for fueling (or refueling) massive black holes, nor the time-scales involved. A particularly interesting problem is the importance of the feedback from a high-luminosity Active Galactic Nucleus (AGN) onto its host galaxy, in the form of huge quantities of ionizing radiation as well as possible mechanical outflows (jets).

Quasar host galaxies have been studied almost exclusively by imaging (e.g., Bahcall et al. 1997, Stockton et al. 1998, Márquez et al 2001). Recent Hubble Space Telescope optical studies have established that high-luminosity quasars generally reside in big ellipticals, irrespective of radio properties (McLeod & Rieke 1995, Disney et al. 1995, Hughes et al. 2000). There also seems to be a

Send offprint requests to: G. Letawe

* based on observations made with ANTU/UT1 at ESO-Paranal observatory in Chile (program 65.P-0361(A)), and with the ESO 3.5m NTT, at La Silla observatory (program 62.P-0643(B)).

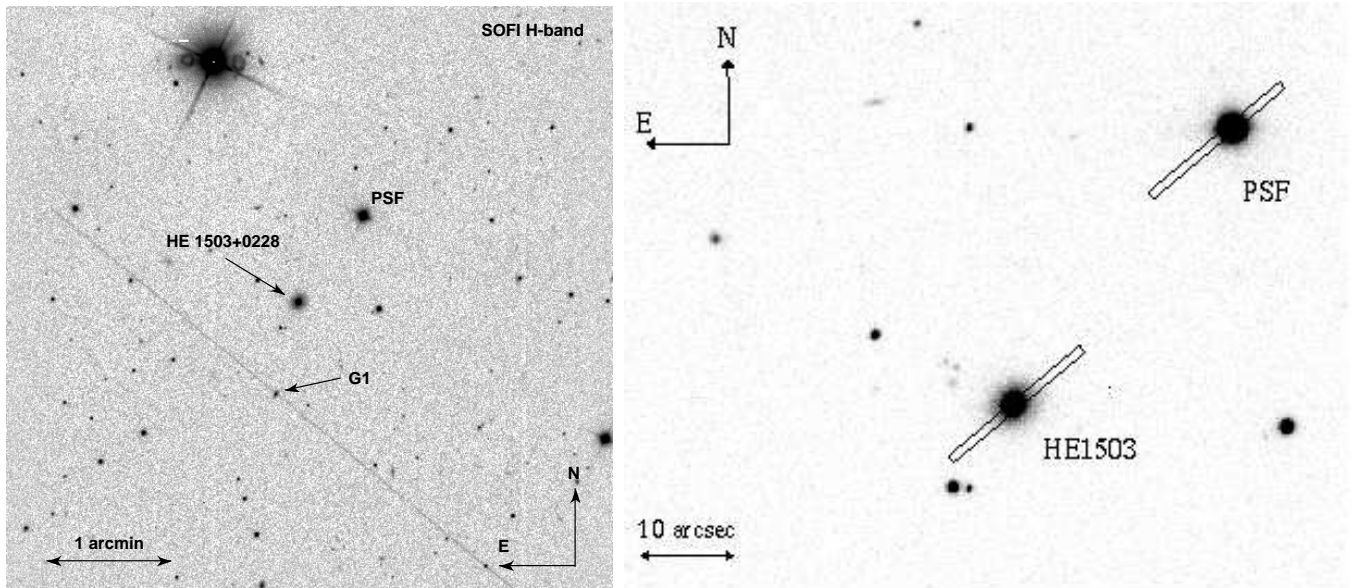


Fig. 1. *Left:* field of view of $5' \times 5'$ around HE 1503+0228. The exposure (H -band) is 480 sec long. It has been obtained with SOFI on the ESO 3.5m NTT. The seeing is $0.8''$ sampled with a $0.29''$ pixel. *Right:* part of the VLT/FORS1 pointing image. The seeing is $0.62''$ on this 30sec R -band exposure. The $1''$ slits used to obtain the spectra of the target and of the PSF star are indicated.

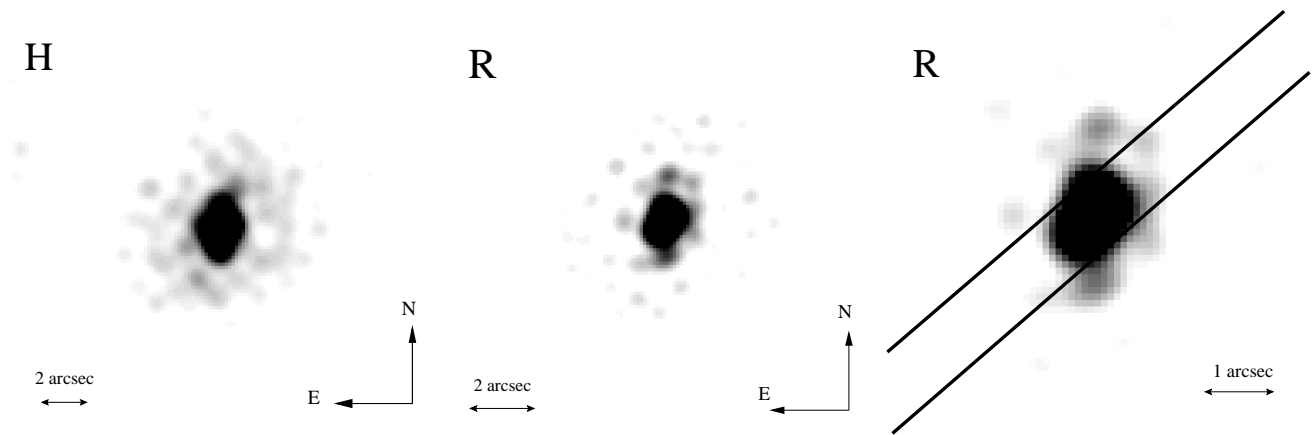


Fig. 2. *Left and middle:* deconvolved NTT and VLT images, where the quasar has been removed from the data. *Right:* zoom on the host galaxy and position of the slitlet used to obtain the spectroscopic data.

trend that more luminous QSOs are hosted by more massive galaxies (McLure et al. 1999, McLeod & Rieke 1995).

A more detailed understanding of the physical conditions in host galaxies can only be obtained from spectroscopic observations. Available evidence in this field is extremely scarce, and although extensive quasar host spectroscopy was conducted already in the early 1980s (e.g., Boroson et al. 1985), they have never really been followed up with improved instrumentation and analysis techniques, except for a few isolated objects (among them 3C 48 being the probably best-studied case in this field – e.g., Chatzichristou et al. 1999, Canalizo & Stockton 2000). Particularly important is the fact that nearly all these observations up to now were designed as “off-nuclear” spectroscopy, avoiding the strong contami-

nation from the AGN itself, but yielding only information on the host for distances of $\gtrsim 5 - 10$ kpc from the nucleus.

With the aim of studying the stellar and gas content of quasar host galaxies, as well as their dynamics, we have initiated a spectroscopic campaign with the ESO-VLT to observe a sample of luminous radio-quiet quasars at low redshift. The sample is based on the Hamburg/ESO Survey (HES; Wisotzki et al. 2000), a wide-angle (~ 7500 deg²) search for optically bright ($B \lesssim 17.5$) quasars in the southern sky. This survey is particularly suited to provide samples for host galaxy studies, mainly because of two reasons: (1) because of its bright limiting magnitude, the survey yields low-redshift quasars in large numbers, (2) the selection does not encompass morphological criteria, i.e., there is no limitation to point sources as in most other optical quasar surveys. This fact and the wide range

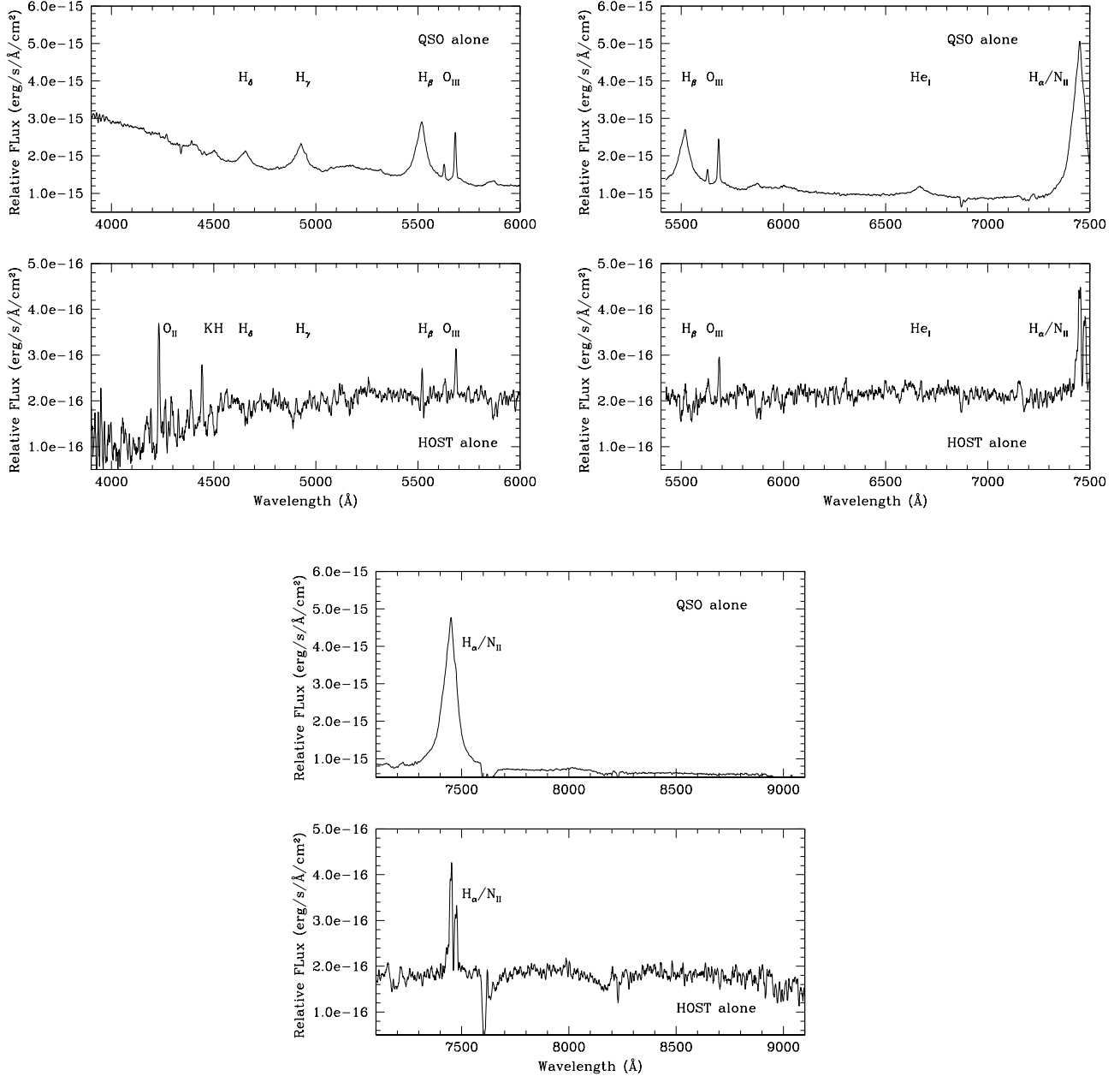


Fig. 3. One dimensional deconvolved spectrum of HE 1503+0228 and its host galaxy. Each panel corresponds to one FORS1 grism and displays the individual flux calibrated spectrum of the quasar and its host alone. Note that the host spectrum shows no trace of the AGN broad emission lines, that are seen narrow in the host galaxy. Note also the very good agreement in the deconvolution of the 3 grisms in the overlapping regions.

of selection criteria employed in the HES (cf. Wisotzki et al. 2000) ensure that quasars are selected irrespective of morphological properties of their host galaxies (see also Köhler et al. 1997). Our objects all have $M_B < -23$ and $z < 0.33$.

The present paper is aimed at exposing the techniques used to obtain high quality spectra of quasar hosts, decontaminated from the contamination by the quasar, and to show their application to one object, taken as a test case: HE 1503+0228, at $z = 0.135$.

2. Observations – data reduction

2.1. Imaging

We have obtained *H*-band images of HE 1503+0228, at La Silla observatory (ESO, Chile) on the night of 1999 February 24th. SOFI was used, the near-IR imager of the 3.5m ESO New Technology Telescope (NTT). The pixel size was $0.29''$ and numerous dithered images of the field were taken in order to produce a combined sky subtracted frame with a total exposure time of 480 sec and a final

mean seeing of $0.8''$. The image is displayed on the left panel of Fig. 1. It shows the environment of the quasar on a $5' \times 5'$ field, with no obvious companion.

Additional data were obtained with the first of the four 8.2m telescopes (UT1) at Paranal observatory. A shallow 30s *R*-band image was taken, in order to design the spectroscopic mask. The seeing was $0.62''$, sampled with a pixel scale of $0.2''$.

Both the near-IR and optical images were deconvolved using the MCS deconvolution algorithm (Magain et al. 1998). While one single optical image of HE 1503+0228 was obtained, many dithered IR images were available in the *H*-band. Eight stacks of images were produced with the data and simultaneously deconvolved as explained in Courbin et al. (1998). This procedure allows for better decomposition of the data into a sum of point source and “background” channels, hence a better extraction of the image of the host, uncontaminated by the AGN’s light. The deconvolved data are shown in Fig. 2, where the quasar has been subtracted.

The photometry of the host of HE 1503+0228 has been performed on the deconvolved images, in a $10''$ diameter aperture. The magnitudes we infer in that way are $R = 16.78 \pm 0.20$ and $H = 14.57 \pm 0.20$.

Determining the shape of the galaxy is of importance as the inclination of the disk component in the mass model (see next sections) depends on the observed galaxy shape, hence affecting the mass determination of the galaxy. We make the assumption that the galaxy has an intrinsic circular geometry, to turn the fitted ellipticities into an inclination angle. Given the relatively low signal-to-noise of our images we chose to determine the shape of the host by fitting analytical profiles to the data (Kuhlbrodt et al. in preparation). Our model is composed of a nucleus, a disk, and a spheroid, convolved with the observed PSF before any fitting is performed. In the case of HE 1503+0228 the spheroid is used to model a bar-like feature in the center of the galaxy, that may affect the fit of the disk component if it were not taken properly into account.

The analysis yields the Position Angle ($PA=38^\circ \pm 3^\circ$) of the host, its inclination ($i = 32^\circ \pm 2^\circ$), and the angle ($\phi = 12 \pm 3^\circ$) between the slit and the major axis of the galaxy. These values are in fact very close to the values found just by measuring the outmost isophotes in the VLT images.

2.2. Spectroscopy

The spectroscopic data were taken on the night of 2000, April 11th with FORS1 mounted on Antu, the first of the four 8.2m VLT Unit Telescopes at Paranal observatory (ESO, Chile). Three gratings were used (G600B, G600R, G600I) to cover the whole optical spectral range 4000-9500Å with a mean spectral resolution of about 700. The seeing during the observations was good, about $0.6''$. Each grism was exposed 1200 sec, under photometric conditions and dark time, which yields a mean S/N of about 150-

200 per pixel (quasar+host). The large pixel size of the detector was used, $0.2''$.

We show in the right panel of Fig. 1 and in Fig. 2 the orientation of the slitlets relative to the quasar host and to the PSF star. In Fig. 2, the images have been deconvolved and the quasar has been removed from the data. The FORS mask consists of 19 slitlets with fixed length and width ($19'' \times 1''$). One slit was centered on HE 1503+0228, one slit was centered on a bright PSF star and the rest of the slits were used either to observe fainter PSF or galaxies. Galaxy G1 is indicated in Fig. 1. It is at $z \sim 0.3$ and is unrelated to the quasar.

At the adopted spectral resolution, the area accessible on the CCD without losing spectral information at the edges of the array is restricted to a strip of sky about $40''$ wide. As we have to observe simultaneously the quasar and at least one PSF star, the PA of the mask is therefore imposed to us by the instrumental design, i.e., the $40''$ strip of sky has to include both the quasar and the PSF star(s). This means that the slitlet centered on the quasar is not necessarily oriented along one of the axes of symmetry of our targets. It also means that we do not observe at parallactic angle. This is however not a major problem as FORS1 has an efficient atmospheric refraction corrector and the data remain unaffected by slit losses.

A two-dimensional wavelength calibration was applied in order to correct for slit curvature, followed by a two-dimensional sky subtraction. The spectrum of HE 1503+0228 and of the PSF star were reduced exactly in the same way, and they were rebinned to a common pixel size of 1\AA in the spectral direction. They were also rebinned to a common starting wavelength, which ensures that to each spectral resolution element of the quasar, corresponds the same spectral resolution element in the PSF.

3. Extraction of the host’s spectrum

Most current spectroscopic studies of quasar host galaxies are designed as off-axis observations, with the slit of the spectrograph placed one to several times the size of the seeing disk away from the center of the AGN (e.g., Hughes et al. 2000).

While such an observational strategy is minimizing contamination by the quasar, it has severe drawbacks. First, one can only study the outer parts of the galaxy. This is limiting the study to particular regions of the hosts. It also requires very long exposure times on large telescopes to detect the extremely faint wings of the hosts. Second, all velocity information is lost, as is the spatial information in general, along the galaxy’s axes of symmetry. Finally, the method is still restricted to the most extended objects and does not allow a full decontamination of the quasar’s light.

Instead, our observations are taken on-axis, placing the slit of the spectrograph on the quasar’s center of light. This avoids all drawbacks of the off-axis observations, but requires clean post-processing techniques in order to remove accurately the spectrum of the AGN. For this pur-

pose we use the spectroscopic version of the MCS deconvolution algorithm (Magain et al. 1998, Courbin et al. 2000). Using the *spatial* information contained in the spectrum of PSF stars located close to the object of interest, the algorithm sharpens the data in the spatial direction, sub-samples them in order to achieve smaller pixel size, and decomposes them into two channels containing (i) the spectrum of the AGN and (ii) the two-dimensional spectrum of the host galaxy.

In the deconvolved spectrum, the new sub-sampled pixel size is $0.1''$ and 1\AA in the spectral direction. In Fig. 3 are displayed the one dimensional flux calibrated spectra, integrated along the spatial direction on the deconvolved data. Interestingly, the three FORS1 grisms have significant regions of overlap that are in perfect agreement with one another. In addition, at the redshift of HE 1503+0228, most emission lines are present in two grisms. This allowed us to construct a combined 2-D flux calibrated spectrum. All measurements presented in this paper, except for velocity curves, are done on the final combined spectrum.

4. Dynamics of the host galaxy

4.1. Redshift

From the different emission lines of the quasar and of the galaxy, we can extract a sharp value for the redshift of HE 1503+0228, by simple Gaussian fitting. The lines of the host galaxy in the deconvolved spectrum have to be measured with particular care: in the center of the host, the lines are double, due to the velocity field of the galaxy and to the deconvolution method. This is mainly due to the extreme contrast between the narrow emission lines of the host, and the broad lines of the quasar: some of the flux in the sharpest parts of the host's emission lines is taken in the point-source component (the quasar) of the deconvolved spectrum, i.e., the central parts of the lines are dimmed. We have therefore taken the mean wavelength between the two sides of emission lines, when measuring the host's redshift. The results for each line are given in table 1. The details of the individual emission lines is accessible via a method described in Section 4.2, which does not alter the center of the lines.

4.2. Velocity curves: extraction method

In the spectroscopic version of the MCS algorithm (Courbin et al. 2000), the difference in spatial properties between the AGN (point source) and the host galaxy (extended component) is used to separate the spectra of these two sources. A smoothing in the spatial direction is applied for this purpose to the extended component. While such a decomposition method is well suited to most spectral regions of the host, it is not optimal for deriving velocity curves: spatial smoothing (which is not precisely known as it varies with the local S/N) may modify the spectral position of the lines at a given spatial position, by averaging spatial components of different radial velocities.

Table 1. Redshift of HE 1503+0228, as inferred from the emission lines of the host galaxy alone, and from the quasar alone. The redshifts are the same for the quasar and for its host.

Line	Redshift (host only)	Redshift (quasar only)
OII (3727Å)	0.1353	0.1352
H β (4861Å)	0.1357	0.1352
OIII (4959Å)	0.1362	0.1349
OIII (5007Å)	0.1356	0.1348
OI (6300Å)	0.1355	0.1352
NII (6548Å)	0.1352	–
H α (6563Å)	0.1353	0.1352
NII (6583Å)	0.1354	–
SII (6716Å)	0.1356	0.1343
Mean	<0.1355>	<0.1350>
Mean error	(± 0.0003)	(± 0.0003)

We have devised another method which is better suited for extracting radial velocity curves of the host galaxy. Instead of using the difference in *spatial* properties to extract the spectra, we take advantage of the different *spectral* properties of the AGN and host to determine the radial velocity as a function of distance.

The fact that the spectral lines of the host are much narrower than any feature in the AGN spectrum is used to determine the spectral position and intensities of the host spectral lines as a function of spatial position. More specifically, at each spatial coordinate we fit the sum of a Gaussian profile of variable width representing the host emission line, plus a smooth numerical curve accounting for the AGN spectrum plus the continuum of the host.

In doing this fit, we also take advantage of the constant shift in wavelength between two given emission lines: several emission lines are fitted simultaneously under the constraint that they are separated by a fixed gap in wavelength. Thus, when we refer to the H α velocity curve, we in fact use the H α and [NII] emission lines simultaneously. Similarly, the H β curve is obtained from the H β and the [OIII] (5007Å) lines, simultaneously. An example of such an extraction is displayed on Fig. 4.

In converting the wavelength shifts into velocity curves, we take several effects into account:

- (1) The orientation of the slit does not coincide with the major axis of the galaxy. This is due to observational constraints, i.e. the fact that we had to obtain the spectrum of a PSF star simultaneously with the quasar and host (see Section 2.2).
- (2) The slit width is comparable to the angular size of the galaxy. The observed wavelength shifts are thus averages of velocity components coming from many parts of the galaxy.
- (3) The galaxy is not seen edge-on, but with an inclination angle i . Radial velocities have thus to be divided by $\sin i$ to be transformed into rotation velocities.

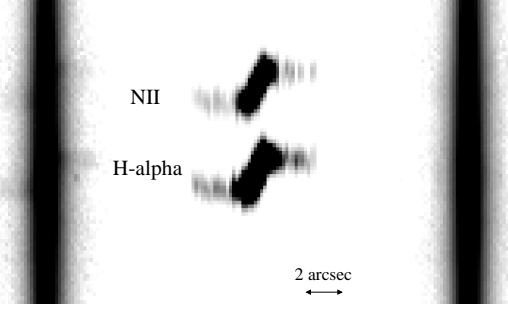


Fig. 4. Example of emission lines extraction. Here are the $H\alpha$ and $[NII]$ emission lines in I -band grism. The left part shows a zoom on initial reduced spectrum. The middle one shows the emission lines alone whereas the right part shows the quasar and galactic continuum.

- (4) The radial velocity curves are smeared by convolution with the seeing profile, both in spatial and spectral directions.

The procedure we use assumes a simple analytical mass model for the host galaxy, which includes a thin disk, a spherical dark matter halo, and a central point mass. The velocity at a distance r away from the galaxy's center is then given by:

$$V_{\text{mod}}(r) = \sqrt{-r(F_{\text{disk}} + F_{\text{dark}} + F_{\text{CM}})} \quad (1)$$

The radial forces in equation (1) are computed using a Kuzmin potential for the disk:

$$F_{\text{disk}}(r, z) = -\frac{r^2 G M_{\text{disk}}}{(r^2 + (a + |z|)^2)^{\frac{3}{2}}} \quad (2)$$

where we assume $z = 0$, hence neglecting the thickness of the disk. M_{disk} is the total mass of the disk and a measures its scale length.

Dark matter is assumed to be spherically symmetrical about the galaxy's center. The force it creates at the distance r away from the center, given a radially dependent density distribution is:

$$F_{\text{dark}}(r) = -\frac{4\pi G \rho_0 r_0^3}{r} \left(\frac{r}{r_0} - \arctan \frac{r}{r_0} \right) \quad (3)$$

where r_0 is the scale length for the mass distribution within the dark matter halo and ρ_0 its central density (Binney & Tremaine 1987).

The force from the central mass M_{cm} is simply

$$F_{\text{CM}}(r) = -\frac{G M_{\text{cm}}}{r} \quad (4)$$

The five parameters M_{disk} , a , ρ_0 , r_0 and M_{cm} are determined by a least squares fit to the data, i.e., to the measured velocity shifts at each spatial pixel along the slit. We therefore minimize the following χ^2 :

$$\chi^2 = \sum_{j=1}^N \frac{1}{\sigma_j^2} \{ (s * V_{\text{mean}})_j \sin i - d_j \}^2 \quad (5)$$

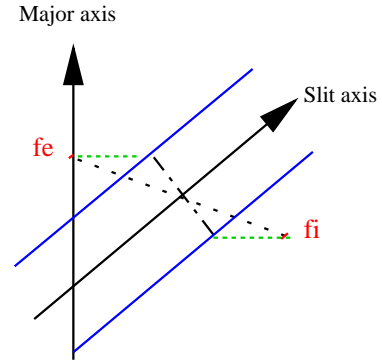
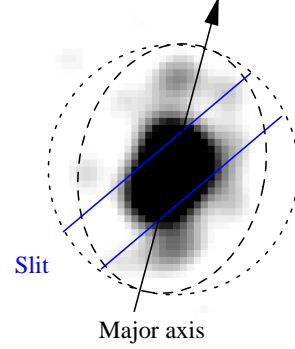


Fig. 5. Schematic illustration of geometrical effects considered for deriving the velocity curves. *Top* : the original face-on galaxy is assumed to be circular (dotted line). Seen with an inclination i , it appears elliptical (dashed line). In addition, the slit is not aligned with the major axis of the inclined galaxy. *Bottom* : The mean velocity at one position along the slit, which would be integrated along a line perpendicular to the slit (dashed-dotted line) if the galaxy was seen face-on, has now to be integrated along a line which is inclined (and lengthened) with respect to the slit (dotted line; see text).

where N is the total number of pixels along the slit, and where $d_j \pm \sigma_j$ is the measured radial velocity shift at pixel j along the slit. V_{mean} is a one dimensional vector that contains the mean (see next paragraph for the significance of “mean”) velocity predicted by our mass model at pixel j along the slit. Due to the seeing, this velocity is affected by blurring in the spatial direction, hence the need for the convolution by the 1 dimensional PSF s obtained from the spectrum of stars. As the galaxy has an inclination i , we multiply the result of the convolution by $\sin i$ before comparing with the observed velocity d_j . The error σ_j on the radial velocity measurements is estimated by comparing the measured d_j for the same emission lines in different grisms. This was possible for the $H\alpha$, $[NII]$, $H\beta$ and $[OIII]$ emission lines.

All the calculations in Eq. 5 assume that the galaxy is seen face-on, the inclination being taken into account by the $\sin i$ term. Due to the non-zero angle ϕ between the slit and the major axis of the galaxy, the velocity in Eq. 5

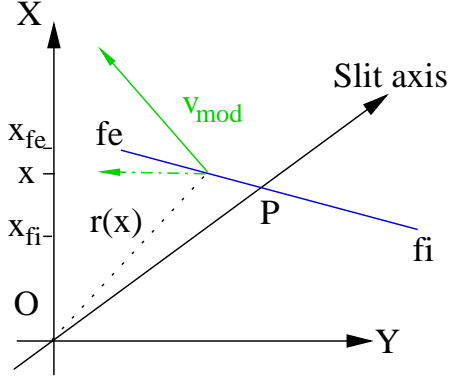


Fig. 6. Description of the integration domain for the computation of $V_{\text{mean}}(P)$. The major axis of the galaxy is along X. f_e and f_i are the limits of the integral also shown in Fig. 5. Only the component of the model velocity V_{mod} along the Y axis contributes to the integral when the galaxy is seen inclined.

is a weighted mean V_{mean} of several velocity components across the slit.

For each pixel j along the slit, lets say at point P (see Fig. 6), one can compute a mean velocity as follows:

$$V_{\text{mean}}(P) = \frac{1}{I_{\text{tot}}} \int_{X_{f_i}}^{X_{f_e}} I[r(x)] \cdot V_{\text{mod}}[r(x)] \cdot \frac{x}{r(x)} \cdot dx \quad (6)$$

$V_{\text{mean}}(P)$ is the average of all the velocity components located along the dash-dotted line in Fig. 5. If the galaxy was seen face-on (as we would like it to be in Eq. 5), this line would be rotated and lengthened, and mapped onto the dotted line of Fig. 5. The integral in Eq. 6 runs along this dotted line. Its equation (Eq. 7) is easily obtained from geometrical considerations, given the inclination i of the galaxy with respect to the plane of the sky and given the orientation ϕ of the slit relative to the major axis of the galaxy:

$$y = \frac{\cos \phi}{\cos i} \left(x - \frac{x_P}{\cos \phi} \right). \quad (7)$$

x_P is the coordinate of the point P on the major axis X (Fig. 6) of the galaxy.

The integration in Eq. 6 is then performed as follow: for each position x along the major axis of the galaxy, we calculate the distance $r(x)$ from the galaxy's center O to the point of the integration line that is considered. This distance is used to weight each velocity component $V_{\text{mod}}[r(x)]$ of the velocity model, according to the light distribution of the galaxy in the emission line. We have estimated the light distribution $I(r)$ of the galaxy, assuming it is intrinsically symmetrical about the center of the galaxy. We model it by fitting a Moffat profile to the 1-dimensional intensity profile along the emission line, and applying deprojection (note that the fit of the emission line is one-dimensional, but since $I(r)$ is known analytically, one can compute weights in 2 dimensions when calculating the integral in Eq. 6). When doing the fit, the

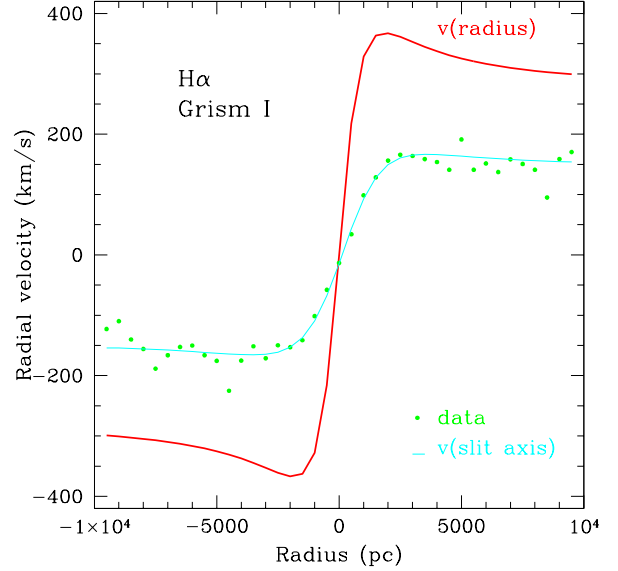


Fig. 7. Inclination/seeing corrected velocity curves for the H α and [NII] emission line (*I*-grism only): the dots show the velocity measurements. The solid line superposed is the fit of our three components model after taking into account misalignment between the slit and the major axis of the galaxy (see text). This solid line shows the variation of V_{mean} along the slit. It is then corrected for inclination and seeing, following Eq. 5, to give the true velocity as a function of distance to the center of the galaxy.

Moffat profile is convolved with the PSF. Correct normalisation is assured by I_{tot} : the total flux of the regions contributing to the measured emission at position P along the slit.

The term $\frac{x}{r(x)}$ in Eq. 6 is the projection of the rotation velocity on the minor axis of the galaxy, which will give rise to a radial velocity once inclination is taken into account. The component of the velocity along the X-axis does not contribute to the mean velocity calculation, once inclination has been taken into account.

The intersections between the integration line and the slit edges, f_i and f_e , give us the limits of the integration, as shown in Figs. 5 and 6).

An example of a inclination/seeing-corrected velocity curve is given in Fig. 7 for the H α /N[II] lines. In our calculations of the linear scales and distances we have used $H_0 = 65 \text{ km.s}^{-1} \text{ Mpc}^{-1}$, $\Lambda = 0$, and $\Omega_M = 0.3$, leading to a scale of $1'' = 2.5 \text{ kpc}$.

4.3. Velocity curves: results

We give in Table 2 the best fit for the 5 parameters of our mass model. The mean velocity curve, as extracted from the H α and H β lines is displayed in Fig. 8. This mean corresponds to four independent curves obtained for the H α and the H β lines, both seen in two different grisms.

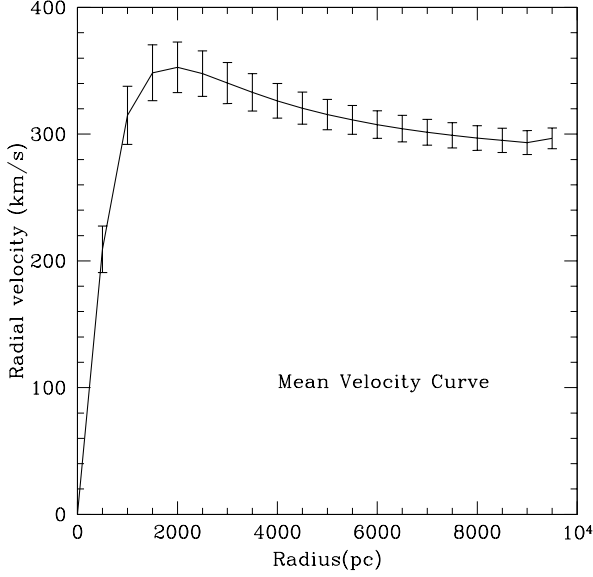


Fig. 8. Mean velocity curve between four models fitted on the H α line (2 grisms) and on the H β line (2 grisms). The error bars are derived from the dispersion between the four curves. The result is corrected for seeing and slit effects, as well as for inclination.

Table 2. Mass model parameters for our velocity curves in each individual grism and for each emission line. a and r_0 are in parsec, ρ_0 in M_\odot/pc^3 and M_{disk} and M_{cm} in M_\odot .

Line	Grism	a	M_{disk}	ρ_0	r_0	M_{cm}
H α	R	1088	$7.9 \cdot 10^{10}$	0.30	2033	$6.1 \cdot 10^7$
H α	I	1163	$8.6 \cdot 10^{10}$	0.31	2074	$4.8 \cdot 10^7$
H β	B	908	$4.8 \cdot 10^{10}$	0.56	1753	$3.5 \cdot 10^6$
H β	R	1428	$5.9 \cdot 10^{10}$	0.23	2196	$2.5 \cdot 10^5$

Table 3. Weighted means of the masses obtained in Table 2 where the weights are computed from the residuals of each individual fit. M_{tot} is the sum of M_{disk} and M_{dark} . Units are solar masses.

Masses	$r < 1 \text{ kpc}$	$r < 3 \text{ kpc}$	$r < 10 \text{ kpc}$
M_{disk}	$1.9 \pm 0.3 \cdot 10^{10}$	$5.1 \pm 0.7 \cdot 10^{10}$	$7.0 \pm 0.9 \cdot 10^{10}$
M_{dark}	$1.1 \pm 0.3 \cdot 10^9$	$1.6 \pm 0.3 \cdot 10^{10}$	$1.2 \pm 0.1 \cdot 10^{11}$
M_{tot}	$2.0 \pm 0.3 \cdot 10^{10}$	$6.7 \pm 1.0 \cdot 10^{10}$	$1.9 \pm 0.2 \cdot 10^{11}$

Table 3 gives our mass estimates which are weighted means of the four fits presented in Table 2, the weights being a function of the residuals after modeling of the data obtained in each individual grism. These weights are the same as the ones applied to compute the mean velocity curve of Fig. 8.

We investigate in Table 4 the effect of the error on the inclination of the galaxy and on its PA. Uncertainties on inclination and orientation of the major axis lead to error bars on masses, which are summarized in Table 4.

Table 4. Effect of the error on the inclination ($32 \pm 2^\circ$) and PA ($38 \pm 3^\circ$) of the host galaxy. Results are given for weighted means of 4 velocity curves, as in Table 3, varying the inclination and the PA within their error bars.

Masses (M_\odot)	$r < 1 \text{ kpc}$	$r < 3 \text{ kpc}$	$r < 10 \text{ kpc}$
Inclination			
M_{disk}	$1.9_{+0.2}^{-0.2} \cdot 10^{10}$	$5.1_{+0.6}^{-0.6} \cdot 10^{10}$	$7.0_{+0.8}^{-0.8} \cdot 10^{10}$
M_{dark}	$1.1_{+0.2}^{-0.02} \cdot 10^9$	$1.6_{+0.2}^{-0.1} \cdot 10^{10}$	$1.2_{+0.1}^{-0.1} \cdot 10^{11}$
M_{tot}	$2.0_{+0.2}^{-0.2} \cdot 10^{10}$	$6.7_{+0.8}^{-0.7} \cdot 10^{10}$	$1.9_{+0.2}^{-0.2} \cdot 10^{11}$
Major axis			
M_{disk}	$1.9_{-0.03}^{+0.02} \cdot 10^{10}$	$5.1_{-0.2}^{+0.1} \cdot 10^{10}$	$7.0_{-0.2}^{+0.2} \cdot 10^{10}$
M_{dark}	$1.1_{+0.04}^{+0.1} \cdot 10^9$	$1.6_{-0.01}^{+0.1} \cdot 10^{10}$	$1.2_{-0.05}^{+0.01} \cdot 10^{11}$
M_{tot}	$2.0_{-0.03}^{+0.03} \cdot 10^{10}$	$6.7_{-0.2}^{+0.2} \cdot 10^{10}$	$1.9_{-0.07}^{+0.03} \cdot 10^{11}$

These results should be interpreted with care, as there is a strong correlation between the model parameters and since the adopted model is simpler than reality. However, while the details of the mass distribution within the galaxy remain inaccurate, we can still determine the total mass of dark matter and as well the disk mass enclosed in a given radius.

Given the results in Tables 2, 3 and 4, we infer a mass estimate of $M(r < 1 \text{ kpc}) = (2.0 \pm 0.3) \cdot 10^{10} M_\odot$. The corresponding mass, integrated over 10 kpc is $M(r < 10 \text{ kpc}) = (1.9 \pm 0.3) \cdot 10^{11} M_\odot$. Table 4 shows that an additional error of 10% should be added, due in part to the uncertainty on the PA of the major axis of the host, but mainly to the uncertainty on its inclination.

5. Stellar and Gas Content

One of the primary goals of our study is to infer the characteristics of the stellar population of quasar host galaxies: does the stellar population of HE 1503+0228 match that of a normal galaxy? Where does it lie in the Hubble sequence?

Let us first note that $H = 14.57 \text{ mag}$ corresponds, with the same cosmological parameters used earlier, to an absolute magnitude of $M_H = -24.5 \text{ mag}$. This, in addition to the profile fitting described in the previous sections, indicates a normal early type local spiral galaxy (Bothun et al. 1985; Arimoto & Jablonka 1991). While the photometric data alone already allow to point out a plausible morphological type for the host of HE 1503+0228, spectroscopy is the key to the determination of its stellar content. A few considerations have to be made before looking at the spectral features in any detail.

First, galactic extinction has to be taken into account. The extinction towards HE 1503+0228 is $A_B = 0.217$ corresponding to $E(B-V) = 0.05$ (Schlegel et al 1998). Our spectrum of HE 1503+0228 has been corrected accordingly.

Second, although no velocity standard stars were taken during the observations, the resolution in the R -grism

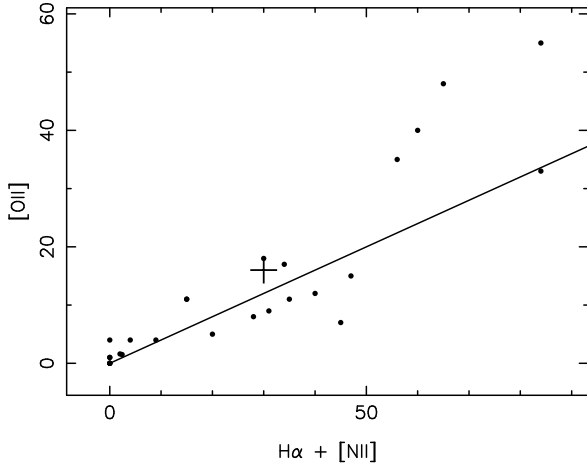


Fig. 9. The relation between the equivalent widths of $H\alpha+[NII]$ and $[OII]$. The black dots show the *normal* spiral galaxies of Kennicutt’s sample. The plain line correspond to $[OII] = 0.4 H\alpha+[NII]$, mean relation of the galaxies dominated by photoionization. The cross indicates the position of HE 1503+0228.

(4.9\AA ; 3.6\AA at rest-frame) is good enough to make use of the stellar library of Jacoby et al. (1984) (FWHM = 3.5\AA). This gives a velocity dispersion of $\sim 170\text{ km/s}$, which we only take as an indicative upper limit value.

Third, we observed HE 1503+0228 with three different grisms, each having a different dispersion. The three spectra were combined in order to cover the wide wavelength range 3670\AA to 9165\AA (3150\AA to 8073\AA once corrected from the redshift $z=0.1355$, or $v=37837.4\text{ km/s}$). In doing this, we have degraded the observations to the resolution of the less resolving grism, i.e., 5.7\AA (or $\sim 5\text{\AA}$ at rest-frame).

Finally, due to the low signal-to-noise ratio of the spectrum in its bluer part, we consider only features from 4000\AA on (3523\AA at rest-frame).

We have only considered the integrated spectrum of HE 1503+0228. In fact, the signal-to-noise of the measurements on each individual spatial resolution element of the 2D data varies between 3 and 6, and therefore does not give much hope in tracing any radial variation in the stellar population, unless deeper data are obtained.

In the following, we measure well known indicators for the underlying stellar populations, for the host of HE 1503+0228, and we compare them with the values obtained for two control samples: the one of Trager et al. (1998) for the elliptical galaxies, and the one of Kennicutt (1992a,b) for the spiral galaxies.

5.1. Emission lines

One of our concern was to verify that the deconvolution procedure had indeed left out any non thermal excitation process.

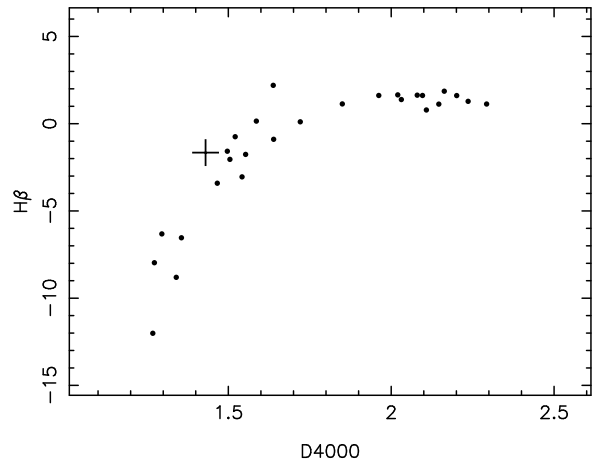


Fig. 10. The relation between the 4000\AA break and the equivalent width of $H\beta$ for normal spiral galaxies (Kennicutt 1992) (dots) and HE 1503+0228 (cross).

We have measured the equivalent widths (EW) of the most prominent emission lines seen in the spectrum of HE 1503+0228, i.e., $[OII]$, $[OIII](4959\text{\AA})$, $[OIII](5007\text{\AA})$ and $H\alpha+[NII]$ (see Table 5).

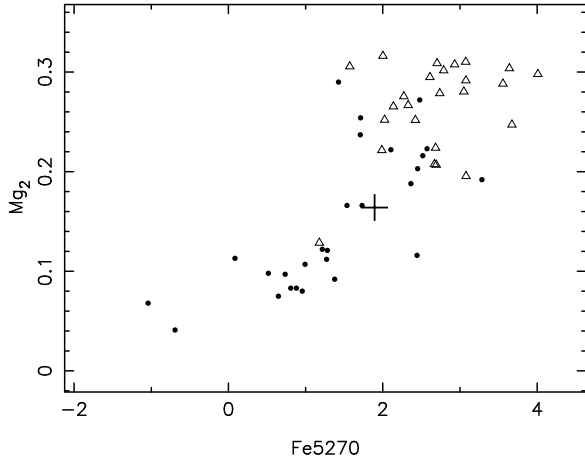
Kennicutt (1992a) provided measurement of the Oxygen lines $[OII]$ (3727\AA), $[OIII]$ (5007\AA) and $H\alpha+[NII]$. He noted that among galaxies with normal star formation rates ($EW(H\alpha+[NII]) \leq 40\text{\AA}$), the $[OIII]$ lines are rarely detected at all ($EW \leq 0.5\text{\AA}$). For HE 1503+0228, while $EW(H\alpha+[NII]) \sim 30\text{\AA}$, we detect $[OIII]$, with an equivalent width of $\sim 4\text{\AA}$. This is the only and discreet sign of an excitation process in or surrounding HE 1503+0228 which is not directly related to star formation and, hence, which might be triggered by the central AGN radiation field. Kennicutt (1992a) also reported that galaxies dominated by stellar photoionization follow a mean relation $EW([OII]) \sim 0.4 EW(H\alpha+[NII])$ (with an rms of 50%). HE 1503+0228 falls nearly exactly on this relation, as shown in Fig. 9. Kennicutt’s galaxies are represented by plain dots, the mean relationship between $H\alpha+[NII]$ and $[OII]$ is the solid line. The position of HE 1503+0228 in this plane is indicated by a cross.

HE 1503+0228 exhibits a weak $[OIII]$ (5007\AA) line. We have left out from the Kennicutt sample the objects which displays strong $[OIII]$ (5007\AA) lines, when analysing in the next section the absorption line features. This ensures that we compare HE 1503+0228 with objects of similar properties.

To further investigate this matter, we have measured the line intensity ratios, $[OIII]/H\beta$ (0.05), $[OIII]/H\alpha$ (0.54), $[NII]/H\alpha$ (-0.20). Due to the deconvolution procedure, the ratios between Oxygen and Balmer lines are upper limits. Indeed, the Balmer lines are probably underestimated. When placed in the diagnostic diagrams of Sodr e and Stasi nska (1999), the host galaxy of HE 1503+0228

Table 5. Lick indices for the spectral features in the host galaxy of HE 1503+0228.

Name	D4000	G4300	Ca4455	Mg ₂	Fe5270	Fe5335	[OIII]	H α + [NII]
Value	1.48	3.41	2.03	0.157	1.89	1.12	4.2	30.
Error	0.04	0.16	0.12	0.002	0.08	0.11	0.3	2.

**Fig. 11.** The relation between the Fe5270 and Mg₂ index for the normal spirals of Kennicutt et al. (1992) (dots) and the ellipticals of Trager et al. (1998) (open triangles). As in Fig. 9 and 10, the cross indicates the position of HE 1503+0228.

falls perfectly on the sequence drawn by the normal spiral galaxies.

To summarize, our analysis of the emission lines suggests that HE 1503+0228 is a perfectly normal spiral galaxy, where the gas emission is dominated by ionization by stars rather than by the central AGN.

5.2. Absorption lines

Our spectra have sufficient signal-to-noise to measure the Lick indices for several stellar absorption features. As the spectral resolution of the Lick system is lower than the resolution of our data, we have convolved the spectrum of HE 1503+0228 with the appropriate Gaussian kernel, in order to match a 200 km s^{-1} rest-frame resolution.

For a full compatibility between the measurements done for HE 1503+0228 and for the galaxy control sample (see previous section), we have re-measured the Lick indices on Kennicutt’s galaxies in exactly the same way as for HE 1503+0228.

A difficulty when looking at the stellar population in HE 1503+0228 is to avoid contamination due to the gas emission. This emission can either “fill-in” absorption lines—the Balmer lines is a well known example, but Mg β can be affected as well (Goudfrooij & Emsellem 1996)—or contaminate the continuum side bands used for the measurements of the equivalent widths. We have identified four absorption lines that are strong enough and free of this

contamination by emission lines. They correspond to the Lick indices G4300, Ca4455, Ca4668, Fe5270 and Fe5335. With only a tiny change in the definition of the continuum window used for the Mg₂ index, we could avoid contamination by the [OIII] (4959Å) emission line for this index. The small change we impose on the continuum side bands produces a change of at most $\pm 0.04 \text{ mag}$ (or 20%) in the measurement of the Mg₂ index. In addition to the indices for the absorption lines, we also measure the important calcium break at 4000Å, which gives the D4000 index (Bruzual 1983).

Table 5 summarizes the results of our measurements. The available signal-to-noise ratio (per Å) for performing the measurements varies between ~ 10 (blue part) and ~ 25 (red part).

The continuum shape of HE 1503+0228 is rather flat, indicative of on-going star formation. Similarly to the result of Fig. 9, Fig. 10 puts HE 1503+0228 among normal spiral galaxies. The latter figure compares the index D4000, which measures the 4000Å break, with the equivalent width of H β which is indicative of the presence of star formation. HE 1503+0228 nicely falls on the sharp relation traced by normal spirals.

As for the chemical abundances, we chose to present in Fig. 11 the Mg₂ and Fe5270 indices. They trace the α and iron peak-elements, respectively. Here again, HE 1503+0228 is located exactly on the Hubble sequence, at the location of spiral galaxies, rather than ellipticals. Furthermore, the values of the absorption line equivalent widths strongly suggests the stellar population of an early type spiral galaxy.

6. Conclusions

We have undertaken a VLT program aimed at unveiling the spectroscopic properties of quasar host galaxies for a sample of radio quiet, bright quasars at low redshift. Our long term scientific goal is double: (1) to compare the stellar populations of quasar hosts with those of other (“normal”) galaxies, and (2) to study their dynamics, as close as possible to the central AGN.

The present paper considers HE 1503+0228 as a test case. An important part of our work is dedicated to the correction of geometrical effects and removal of the atmospheric blurring. This is crucial in the central parts of the galaxy, with sizes comparable to the seeing disk.

We find that the stellar population of the host galaxy of HE 1503+0228 compares well with that of the normal non-AGN spiral galaxies of Kennicutt (1992a,b) and Trager et al. (1998). They show no trace of enhanced star formation. The interstellar medium does not show significant ionization by the central AGN. Its mass $M(r <$

10 kpc) = $(1.9 \pm 0.3)10^{11} M_{\odot}$ also compares very well with that of other spiral galaxies. To summarize, the host galaxy of HE 1503+0228 is a normal spiral galaxy.

Acknowledgements. The authors would like to thank Sandrine Sohy for help with some of the intensive programing involved in this work. Géraldine Letawe is a teaching assistant supported by the University of Liège, (Belgium) and is partially funded by the Pôle d'Attraction Interuniversitaire, P4/05 (SSTC, Belgium). Frédéric Courbin acknowledges financial support through Marie Curie grant MCFI-2001-0242. Chilean grant FONDECYT/3990024 and additional support from the European Southern Observatory are also gratefully acknowledged. Dante Minniti is supported in part by Fondap Center for Astrophysics.

References

- Arimoto, N., Jablonka, P., 1991, A&A 249, 374
 Bahcall J.N., Kirhakos S., Saxe D.H., Schneider D.P., 1997, ApJ 479, 642
 Binney J., Tremaine S., 1987, Galactic Dynamics, Princeton: Princeton Series in Astrophysics
 Boroson T. A., Persson S. E., Oke J. B., 1985, ApJ 293, 120
 Bothun G.D., Mould J., Schommer R.A., Aaronson M., 1985, ApJ 291, 586
 Bruzual A.G., 1983, ApJ 273, 105
 Canalizo G., Stockton A., 2000, ApJ 528, 201
 Chatzichristou E.T., Vanderriest C., Jaffe W., 1999, A&A 343, 407
 Courbin F., Lidman C., Magain P., 1998, A&A 330, 57
 Courbin F., Magain P., Kirkove M., Sohy S., 2000a, ApJ, 539, 1136
 Disney M. J., Boyce P. J., Blades J. C., 1995, Nature 376, 150
 Goudfrooij P., Emsellem E., 1996 A&A 306, 45
 Hughes D.H., Kukula M.J., Dunlop J.S., Boroson T., 2000, MNRAS 316, 204
 Jacoby G. H., Hunter D. A., Christian C. A., 1984, ApJS 56, 257
 Kennicutt R.C., 1992a, ApJS 79, 255
 Kennicutt R.C., 1992b, ApJ, 388, 310
 Kuhlbrodt B., et al., in preparation
 Köhler T., Groote D., Reimers D., Wisotzki L., 1997, A&A 325, 502
 McLeod K. K., Rieke G. H., 1995a, ApJ 454, L77
 McLeod K. K., Rieke, G. H., Storrie-Lombardi, L. J., 1999, ApJ 511, L67
 McLure R. J., Kukula M. J., Dunlop J. S., et al. 1999, MNRAS 308, 377
 Magain P., Courbin F., Sohy S., 1998, ApJ, 494, 452
 Magorrian J., Tremaine S., Richstone D., et al. 1998, AJ 115, 2285
 Marquez I., Petitjean P., Theodore B., et al. 2001, A&A 371, 97
 Percival W. J., Miller L., McLure R. J., Dunlop J. S., 2001, MNRAS 322, 843
 Schlegel D.J., Finkbeiner D.P., Davis M., 1998, ApJ 500, 525
 Sodr e L., Stasińska G., 1999, A&A 345, 391
 Stockton A., Canalizo G., Close L., 1998, ApJ 500, L121
 Trager S.C., Worthey G., Faber S.M., et al. 1998, ApJS 116, 1
 Vogt N., Forbes D., Phillips A., Gronwall C., Faber S. Illingworth G., Koo D., 1996, ApJ 465, L15-L18
 Wisotzki L., Christlieb N., Bade N., et al., 2000, A&A 358, 77